





# Real-Time Capable Thermal Model of an Automotive Permanent Magnet Synchronous Machine

MARTIN STEFAN BAUMANN <sup>1</sup>, ANDREAS STEINBOECK <sup>1</sup>,  
WOLFGANG KEMMETMÜLLER <sup>1</sup> (Member, IEEE), AND ANDREAS KUGI <sup>1,2</sup> (Senior Member, IEEE)

<sup>1</sup>Automation and Control Institute (ACIN), TU Wien, 1040 Vienna, Austria

<sup>2</sup>AIT Austrian Institute of Technology, 1210 Vienna, Austria

CORRESPONDING AUTHOR: MARTIN STEFAN BAUMANN (e-mail: baumann@acin.tuwien.ac.at).

**ABSTRACT** Excessive temperatures can lead to accelerated aging and irreversible damage in electric machines. Therefore, real-time temperature monitoring is vital for highly utilized electric machines in automotive drives to ensure that temperatures are within safe operating limits during operation. Installing temperature sensors on all critical parts would incur too much cost. Hence, model-based real-time temperature monitoring is a preferred solution. Recent publications typically utilize low-dimensional lumped-parameter thermal networks. This article presents a modeling method for a permanent magnet synchronous machine (PMSM), where the thermal model is derived using the finite-volume method. The model is calibrated with measurement data. A model-order reduction method is applied, which significantly reduces the computational costs of the model while preserving important (uncertain) parameters, such as heat transfer coefficients. Experimental results for different load cycles of the considered machine validate the feasibility and accuracy of the proposed model. Finally, comparing the model with measured temperatures at positions not used for calibration shows that the proposed method accurately captures the temperature distribution in the whole machine without changing the model structure.

**INDEX TERMS** Model-order reduction, permanent magnet synchronous machine (PMSM), temperature estimation, temperature monitoring, system identification.

## I. INTRODUCTION

Due to their high power density, permanent magnet synchronous machines (PMSMs) are widely used in automotive traction drives. Elaborate cooling concepts have been developed [1] to maximize power density and keep temperatures within safe limits. However, short-time operation above the stationary thermal limits is frequently required. An excessive temperature in parts, such as winding or permanent magnets, can lead to insulation failure or demagnetization of permanent magnets, thereby irreversibly damaging the machine [2], [3]. Thus, accurate knowledge of the temperature distribution within the PMSM is required to ensure its safe operation. Temperature sensors on these parts, especially in the rotor, would entail high costs and the risk of sensor failure.

Therefore, online model-based temperature estimation has been proposed as an alternative [4].

## A. STATE-OF-THE-ART REVIEW

In the design phase of electric machines, often a combination of finite element analysis (FEA), computational fluid dynamics, and high-dimensional lumped-parameter thermal networks (LPTNs) is used to predict the machine's electrical, mechanical, and thermal behavior [5], [6]. These models have high fidelity but require high computing power and are unsuitable for online temperature estimation [7]. In contrast, LPTNs with a low number of nodes (typically between 2 and 12 nodes, see, e.g., [7] or [8]) are widely used for online temperature estimation. The heat transfer processes and losses are

modeled with equivalent circuits of resistors, capacitors, voltage sources, and current sources. Special equivalent circuit elements were developed for modeling thermal anisotropy and internal heat generation [9]. However, identifying a suitable structure for the thermal network and correctly choosing the geometric dimensions to calculate the resistances are the non-trivial tasks that require significant prior knowledge.

Since these approximations are subject to uncertainties, gray-box LPTNs that are mainly parameterized based on measurements were developed. In [10], physically meaningful ranges for thermal resistances are calculated based on the geometry and material parameters. The particular values are then tuned based on measurements. This approach has the drawback that the identified thermal resistances and capacitances are only partially interpretable as physical parameters. Varying speeds and varying cooling boundary conditions that occur during the operation of electrical machines can be considered in LPTNs in the form of linear parameter-varying models [10]. In [11], a combination of LPTNs and 2-D analytical thermal models is proposed to overcome the limitations of low-order LPTNs resulting from coarse spatial discretization. Finally, methods exclusively based on measurements have been proposed recently [12]. They require minimal a priori knowledge of the machine but a large amount of data. The systematic design of excitation signals to identify all relevant regions of the input and state space in minimal time remains an open question [7].

Another method to derive a real-time capable thermal model of electric machines is given by applying model-order reduction techniques to a high-fidelity model, e.g., [13], [14], [15], and [16]. In [14], a reduced-order model (ROM) is constructed by decomposing the system into a static and a dynamic subsystem. Experimental results for the stator of a liquid-cooled machine using a 35-order model show errors of less than 1.45 °C and computation times allowing real-time implementation. In [15], a linear parameter-varying model with speed as a parameter is constructed. Several linear models for fixed-parameter values are stored and reduced using balanced truncation. Linear interpolation results in a model for parameter values between these set values. The main drawback of this method is that the number of stored models and the computational complexity of the interpolation increase exponentially as the dimension of the parameter space increases. In [13], a method for parametric model-order reduction of bilinear thermal models is presented. However, only a single stator tooth without a rotor is simulated, and the ROM dimensions range from 40 to 300. Essential model parameters, such as heat transfer coefficients, are preserved during the model-order reduction. Simulation results of the ROM show that it agrees with the full-order model (FOM) with errors of less than 0.07 °C. Recently, in [16], a parametric model-order reduction approach similar to [13] has been successfully applied to a finite-element model of a machine with a cooling jacket and oil cooling of the end windings and the rotor. The ROM with 135 states in [16] agrees well with the FOM in

simulation. The unknown heat transfer coefficients were found by individually identifying parameters using steady-state measurement results with different operating conditions. During steady-state operation at up to 40% of the maximum torque, the accuracy of the ROM is within 10 °C.

## B. CONTRIBUTION

While these model-order reduction methods are very promising, they have yet to be validated on a complete machine during transient operation or suffer from escalating complexity as the complexity of the cooling concept and, therefore, the parameter space grows. Thus, this article aims to derive a method that utilizes all available a priori information during the physics-based motor modeling. Essential parameters influencing the heat transfer coefficients are identified using experimental data containing a variety of operating conditions. A model-order reduction similar to [13] is applied to obtain a real-time capable model. Quantities, such as the heat transfer coefficients to coolants, are preserved during the model-order reduction, allowing for variation of, e.g., coolant flow rates and rotational speed, without the need to interpolate multiple local models. It is shown that this reduces the computational complexity and thus is suitable for modeling complex cooling concepts. The developed model is experimentally validated for a complete machine operated at various transient operating conditions and compared with an LPTN model. The main scientific contributions are as follows.

- 1) A parametric model-order reduction method is applied to a finite volume model of the overall machine, resulting in a ROM that preserves important physical parameters of the motor.
- 2) The model is parameterized by a single set of parameters obtained by calibration using measurements that cover the entire steady-state and transient operations in the continuous- and peak-performance range of the motor.
- 3) The model is also validated based on sensors not used for model calibration. This proves the ability of the proposed model to estimate temperatures at locations inaccessible for measurements during calibration.
- 4) The comparison with an LPTN of comparable computational complexity further demonstrates the advantages of the proposed method.

## C. STRUCTURE OF THIS ARTICLE

The rest of this article is organized as follows. Section II develops a finite-volume model for the machine, where certain model parameters that cannot be accurately determined from construction data with sufficient accuracy are obtained during the identification step using measurement results in Section IV-B. The order of the resulting calibrated model is reduced in Section III. A comparison of the FOM and ROM and an experimental validation of the developed model are given in Section IV. Finally, Section V concludes this article.

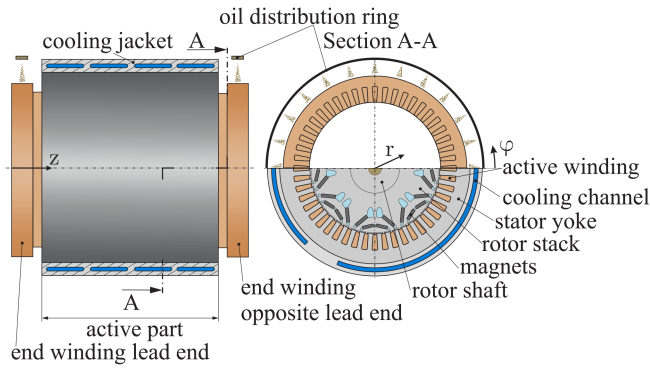


FIGURE 1. Sectional drawing of the machine.

TABLE 1. Main Machine Data

Continuous power	~100 kW
Max. speed	16 500 min <sup>-1</sup>
Stator outer diameter	~230 mm
Stator stack axial length	~130 mm

## II. MATHEMATICAL MODEL

This section presents a physics-based model for the PMSM schematically depicted in Fig. 1.

### A. OVERVIEW OF THE PMSM

The machine consists of a stator that contains slots for the active part of the distributed winding (i.e., the coils span multiple teeth). The wire bundles forming the coils extend axially out of the slots, forming the end windings on the lead end (le) and the opposite lead end (ole) side of the machine. The machine is actively cooled by pumping fluid through the channels in the cooling jacket surrounding the stator yoke. A housing encloses the whole machine. On the cylindrical surface, the cooling jacket is integrated into the housing. Oil distribution rings spanning three-fourths of the circumference spray oil onto the end windings to cool them directly. The rotor contains the permanent magnets embedded into pockets inside the rotor stack. The rotor stack is mounted on a hollow shaft flooded with oil to cool the rotor. The main data of the PMSM are summarized in Table 1.

### B. FINITE-VOLUME MODEL

The heat conduction in a solid can be described by the heat equation, which is a partial differential equation [17]. To approximate the temperature field  $\vartheta$  in the machine, the finite-volume method [18] is applied to the heat equation. Due to the approximately cylindrical shape of radial flux machines, a regular cylindrical grid is used for the discretization, see Fig. 2.

Application of the first law of thermodynamics [17] to one volume  $\mathcal{V}_i$  of the grid yields

$$\int_{\mathcal{V}_i} \rho c_p \dot{\vartheta} dV = \int_{\mathcal{V}_i} g dV - \int_{\partial \mathcal{V}_i} \mathbf{q}'' \cdot \mathbf{n} dA \quad (1)$$

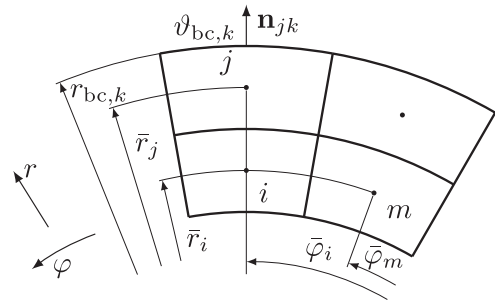


FIGURE 2. Discretization on a regular cylindrical grid.

where  $\rho$  and  $c_p$  are the material's mass density and specific heat capacity, respectively. The power supplied to the volume is described by the heat generated per unit volume  $g$ , and  $\mathbf{q}''$  is the heat flux on the boundary  $\partial \mathcal{V}_i$  of the volume. Furthermore,  $\mathbf{n}$  is the surface normal oriented to the outside of  $\mathcal{V}_i$ . Assuming that the temperature  $\vartheta_i$  and  $g_i$  are uniform within  $\mathcal{V}_i$  yields the finite-volume formulation of (1) as

$$C_i \dot{\vartheta}_i = g_i V_i + \sum_{j=1}^N Q_{ij} \quad (2)$$

where  $C_i = \int_{\mathcal{V}_i} \rho c_p dV$  is the heat capacitance,  $V_i = |\mathcal{V}_i|$  is the volume of  $\mathcal{V}_i$ , and  $N$  is the number of finite volumes. The boundary  $\partial \mathcal{V}_i$  of  $\mathcal{V}_i$  is split up into the surfaces  $\mathcal{A}_{ij}$  shared with neighboring volumes  $\mathcal{V}_j$  and surfaces  $\mathcal{A}_{bc,ik}$  that are part of the boundary.  $Q_{ij} = - \int_{\mathcal{A}_{ij}} \mathbf{n}_{ij} \cdot \mathbf{q}''_{ij} dA = -Q_{ji}$  is the heat flow through the surface  $\mathcal{A}_{ij}$  into  $\mathcal{V}_i$ . Of course, the heat flow  $Q_{ij}$  is nonzero only for neighboring volumes.

Fourier's law [17] gives the heat fluxes that depend on the thermal conductivity  $\lambda$  in the material and contact conductances  $h_c$  at the interface of two different materials. The heat flux  $\mathbf{q}''_{ij}$  between two neighboring elements  $\mathcal{V}_i$  and  $\mathcal{V}_j$  is approximated by finite differences on the cylindrical grid [18] in the finite-volume model (2). This yields

$$Q_{ij} = \frac{A_{ij}}{\frac{\Delta l_{ij}}{2\lambda_{ij}} + \frac{\Delta l_{ij}}{2\lambda_{ji}} + \frac{1}{h_{c,ij}}} (\vartheta_j - \vartheta_i) = G_{ij} (\vartheta_j - \vartheta_i) \quad (3)$$

where  $h_{c,ij}$  is the contact conductance, and  $G_{ij}$  is the effective heat conductance between the volumes. If the volumes are of the same material or there is ideal contact,  $h_{c,ij} \rightarrow \infty$  is used. In general, the thermal conductivity depends on the direction of the heat flux. Therefore, the thermal conductivity of volume  $i$  for a heat flux to volume  $j$  is denoted as  $\lambda_{ij}$ . The grid spacing  $\Delta l_{ij}$  is given by

$$\Delta l_{ij} = \begin{cases} |\bar{r}_j - \bar{r}_i|, & \text{radial direction} \\ \bar{r}_i |\bar{\varphi}_j - \bar{\varphi}_i|, & \text{circumferential direction} \\ |\bar{z}_j - \bar{z}_i|, & \text{axial direction.} \end{cases} \quad (4)$$

If  $\mathcal{A}_{bc,jk}$  is a domain boundary of volume  $\mathcal{V}_j$ , subject to a convective boundary condition with heat transfer coefficient  $h_{jk}$  and temperature  $\vartheta_{bc,k}$ , the heat flow is given analogously

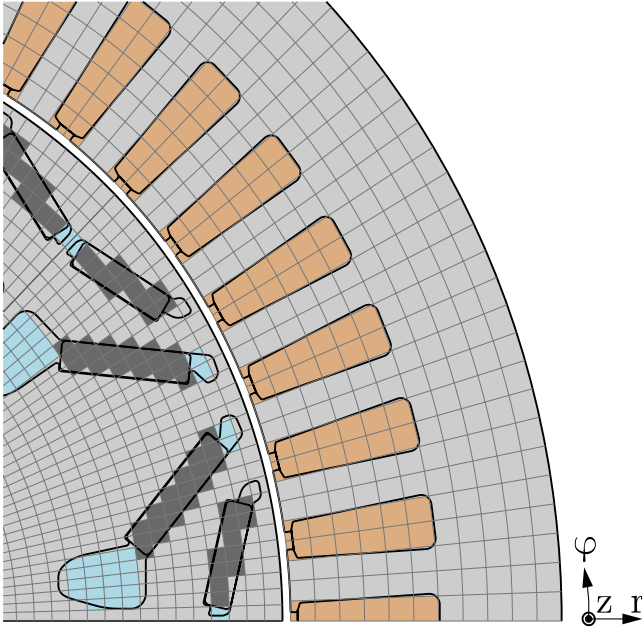


**FIGURE 3.** Discretization of the PMSM with the colors corresponding to the assigned materials: The lamination stack is highlighted in light gray, the active winding is in copper color, the permanent magnets are in dark gray, and the air is in light blue.

in the form

$$Q_{jk} = \frac{A_{bc,jk}}{\frac{\Delta l_{bc,jk}}{\lambda_{jk}} + \frac{1}{h_{jk}}} (\vartheta_{bc,k} - \vartheta_j) = G_{bc,jk} (\vartheta_{bc,k} - \vartheta_j). \quad (5)$$

The spacing for the boundary is given by

$$\Delta l_{bc,jk} = \begin{cases} |r_{bc,k} - \bar{r}_j|, & \text{radial direction} \\ |\bar{r}_j |\varphi_{bc,k} - \bar{\varphi}_j|, & \text{circumferential direction} \\ |z_{bc,k} - \bar{z}_j|, & \text{axial direction} \end{cases} \quad (6)$$

where the dimensions with subscript bc are defined with respect to the boundary, see Fig. 2.

The discretization of the rotor and stator is depicted in Fig. 3. Within this work, the active part of the stator is discretized into 11 volumes in the radial direction and four elements per slot pitch in the azimuthal direction. The radial and azimuthal sizes of the elements are the same for the end windings as for the active part. The rotor is discretized separately with a smaller element size in radial and azimuthal direction to capture the smaller features due to the magnets. There are  $30 \times 30$  elements in the radial and azimuthal direction. In the axial direction, the active part of the stator and the rotor is segmented into three volumes, while a single segment is used for each end winding.

### C. MATERIAL PROPERTIES

Each volume is assigned one of the following materials: lamination stack (ls), active winding (aw), end winding (ew), rotor shaft (rs), permanent magnet (pm), and air (air).

The rotor shaft and the permanent magnet are made of solid material, which renders the thermal conductivity independent of the direction of the heat flow. The parameters  $\rho_{rs}$ ,  $c_{p,rs}$ ,  $\lambda_{rs}$  and  $\rho_{pm}$ ,  $c_{p,pm}$ ,  $\lambda_{pm}$  are taken from datasheets. The magnets are inserted into the rotor with a (small) clearance and are glued in place. This nonideal contact is modeled by a contact conductance between the permanent magnet and the rotor lamination stack similar to, e.g., [19]. The contact conductance is approximated by a uniform gap between the permanent magnet (width  $w_{pm}$ ) and the pocket in the lamination stack (width  $w_{pocket}$ ) of length  $\frac{1}{2}(w_{pocket} - w_{pm})$ . The gap is filled with glue with thermal conductivity  $\lambda_{glue}$ , which yields the contact conductance  $h_{c,pm,ls} = \frac{2\lambda_{glue}}{w_{pocket} - w_{pm}}$ .

The rotor lamination stack is assembled onto the shaft with an interference fit. A typical value for the effective interface gap  $l_{rs,ls}$ , as tabulated in [20], is used to approximate the contact conductance  $h_{c,rs,ls} = \frac{\lambda_{air}}{l_{rs,ls}}$  with the thermal conductivity of air  $\lambda_{air}$ .

The air pockets depicted in Fig. 3 are sealed at the ends of the rotor such that no axial airflow occurs. The pockets are modeled as solid air volumes (i.e., the airflow is neglected) with parameters  $\rho_{air}$ ,  $c_{p,air}$ , and  $\lambda_{air}$ . As the thermal conductivity  $\lambda_{air}$  is small compared with the surrounding material, the finite contact conductance has negligible impact on the overall temperature distribution. Thus, an ideal thermal contact is assumed.

The stator and rotor lamination stack is made of axially stacked steel sheets that are electrically insulated to reduce eddy currents. The stacking significantly reduces the thermal conductivity in the axial direction (ax) compared with the in-plane (pl) thermal conductivity [21]. Given the stacking factor  $k_{st}$  and the thermal conductivity  $\lambda_{ins}$  of the insulation and iron  $\lambda_{Fe}$ , the series connection of insulation and metal sheets with thickness  $1 - k_{st}$  and  $k_{st}$  yields the effective axial thermal conductivity

$$\lambda_{ls,ax} = \left( \frac{(1 - k_{st})}{\lambda_{ins}} + \frac{k_{st}}{\lambda_{Fe}} \right)^{-1}. \quad (7)$$

The in-plane thermal conductivity  $\lambda_{ls,pl} = \lambda_{Fe}k_{st} + \lambda_{ins}(1 - k_{st})$  and the mass density  $\rho_{ls} = \rho_{Fe}k_{st} + \rho_{ins}(1 - k_{st})$  are the weighted average properties. Consequently, the equivalent specific heat capacity is  $c_{p,ls} = \frac{1}{\rho_{ls}}(\rho_{Fe}c_{p,Fe}k_{st} + \rho_{ins}c_{p,ins}(1 - k_{st}))$ .

The active (aw) and end windings (ew) consist of stranded enameled copper wires embedded in an impregnating resin. Modeling the individual strands would cause exorbitant complexity due to the required small discretization volumes. Therefore, the active and end windings are modeled with equivalent homogeneous parameters. For the active and end winding  $x \in \{aw, ew\}$ , the mass density  $\rho_x = \rho_{Cu}k_{x,Cu} + \rho_{res}(1 - k_{x,Cu})$  and the specific heat capacity

$$c_{p,x} = \frac{\rho_{Cu}c_{p,Cu}k_{x,Cu} + \rho_{res}c_{p,res}(1 - k_{x,Cu})}{\rho_x} \quad (8)$$

are calculated according to [22] from copper (Cu) and resin (res) material properties. The fill factor  $k_{x,Cu}$  is the ratio of the conductor volume to the overall active or end winding volume. In the active winding, the wires are oriented axially. The equivalent axial thermal conductivity  $\lambda_{aw,ax}$  is thus modeled as a parallel connection of copper and resin

$$\lambda_{aw,ax} = k_{aw,Cu}\lambda_{Cu} + (1 - k_{aw,Cu})\lambda_{Res}. \quad (9)$$

In [22], several models (such as the Hashin–Shtrikman model) for the equivalent thermal conductivity orthogonal to the axial direction of the conductors are compared with results from finite-element models and experiments. It is shown that analytical models (such as the Hashin–Shtrikman model) typically overestimate the thermal conductivity, especially when the thermal conductivity of the enameling is considerably lower than that of the resin. Since the thermal conductivities for resin and enameling differ by only approximately 20% for the studied motor, the extended Hashin–Shtrikman model [22] is used to estimate the equivalent in-plane (pl) thermal conductivity

$$\lambda_{aw,pl} = \lambda_a \frac{(1 + k_{aw,Cu})\lambda_{Cu} + (1 - k_{aw,Cu})\lambda_a}{(1 - k_{aw,Cu})\lambda_{Cu} + (1 + k_{aw,Cu})\lambda_a} \quad (10)$$

with the equivalent thermal conductivity  $\lambda_a$  of the wire enameling (en) and the resin (res), given by

$$\lambda_a = \frac{\lambda_{res}k_{aw,res} + \lambda_{en}k_{aw,en}}{k_{aw,res} + k_{aw,en}}. \quad (11)$$

The fill factors for enameling  $k_{aw,en}$ , resin  $k_{aw,res}$ , and copper  $k_{aw,Cu}$  sum to one. In the end winding, the wires are oriented mainly in the circumferential direction. Thus, a model of the form (9) is used for the equivalent azimuthal thermal conductivity  $\lambda_{ew,az}$  and a model of the form (11) for the radial  $\lambda_{ew,rad}$  and axial  $\lambda_{ew,ax}$  thermal conductivity.

The equivalent thermal conductivities orthogonal to the wire direction are typically significantly lower than the bulk conductor properties due to the resin between the conductors. They are subject to uncertainty due to, e.g., nonuniform placement of conductors and varying impregnation quality. For the end windings, the unknown exact orientation of the strands introduces a further source of model inaccuracy. Thus, the final value of the thermal conductivities  $\lambda_{aw,pl}$ ,  $\lambda_{ew,ax}$ ,  $\lambda_{ew,rad}$ , and  $\lambda_{ew,az}$  must be obtained by parameter identification, as described in Section IV-B, where (9) and (11) serve as suitable starting points. A slot liner for electrical insulation against the stator stack surrounds the active winding. It is modeled as a thermal contact between the homogenized active winding and the stator stack with contact conductance  $h_{c,aw,ls} = \frac{\lambda_{liner}}{t_{liner}}$ , where  $\lambda_{liner}$  is the thermal conductivity and  $t_{liner}$  is the thickness.

#### D. BOUNDARY CONDITIONS

The stator lamination stack is contained in an aluminum cooling jacket (cj), and the whole cylindrical face of the machine is enclosed by a housing, shielding the machine from ambient

air. The heat transfer over the axial end shields to the ambient air is also small compared with the heat transfer to the water and oil cooling and, thus, neglected in this work. To actively cool the machine, a water–glycol mixture with an inlet temperature  $\vartheta_w$  is pumped at a flow rate of  $q_w$  through a spiral channel in the cooling jacket. For practical water flow rates,  $q_w > 0$ , the heat transfer to the cooling jacket is significantly higher than the heat transfer from the housing to the ambient air. The thermal diffusivity of the aluminum cooling jacket is significantly higher than that of the lamination stack (7). Further, the nonideal contact between the stator lamination stack and the cooling jacket significantly limits the heat that can be transferred from the machine to the cooling jacket [23]. Therefore, the heat capacity and the temperature gradient within the cooling jacket are neglected, and a convective boundary condition with heat transfer coefficient  $h_{ls,o}$  on the radial outer surface of the stator lamination is used. The heat transfer coefficient  $h_{ls,o}$  is composed of the contact conductance  $h_{c,ls,cj}$  between the stator lamination stack and the cooling jacket, and the heat transfer coefficient  $h_{cj}$  from the cooling jacket to the water–glycol mixture is in the form

$$h_{ls,o} = \left( \frac{1}{h_{cj}} + \frac{1}{h_{c,ls,cj}} \right)^{-1}. \quad (12)$$

A typical value for the effective air gap between the cooling jacket and the stator lamination stack is taken from [20] to calculate  $h_{c,ls,cj}$ . The heat transfer coefficient  $h_{cj}$  strongly depends on the flow behavior within the cooling channel (length  $l_{cha}$ , cross-sectional area  $A_{cha}$ , and perimeter  $U_{cha}$ ), see, e.g., [17]. In order to model  $h_{cj}$ , the Reynolds number given by  $Re_w = \frac{v d_h}{\nu_w}$  with the velocity  $v = \frac{q_w}{A_{cha}}$  of the fluid and the hydraulic diameter  $d_h = \frac{4A_{cha}}{U_{cha}}$  as well as the Prandtl number  $Pr_w$ , the thermal conductivity  $\lambda_w$ , and the kinematic viscosity  $\nu_w$  of the water–glycol mixture are required. These temperature-dependent parameters are evaluated at the temperature  $\vartheta_w$  by performing linear interpolation between values tabulated in [24]. The heat transfer coefficient in the channel is calculated by Nusselt relations [17] for the laminar and turbulent flow regimes. For Reynolds numbers  $Re_w > 4000$ , the Nusselt number reads as

$$Nu_{cj,turb} = \eta_1 \frac{\xi}{8} \frac{(Re_w - 1000) Pr_w}{1 + 12.7 \sqrt{\frac{\xi}{8}} \left( Pr_w^{\frac{2}{3}} - 1 \right)} \quad (13)$$

with the friction factor  $\xi$  approximated by [17]

$$\xi = (0.79 \ln Re_w - 1.64)^{-2}. \quad (14)$$

For laminar flow with  $Re_w < 2300$ , the Nusselt number takes the form [17]

$$Nu_{cj,lam} = \eta_2 \left( 3.66 + \frac{0.0668 \frac{d_h}{l_{cha}} Re_w Pr_w}{1 + 0.04 \left( \frac{d_h}{l_{cha}} Re_w Pr_w \right)^{2/3}} \right). \quad (15)$$

Parameters  $\eta_1$  and  $\eta_2$  are introduced to adjust the model to measurements, where  $\eta_1 = \eta_2 = 1$  accounts for the nominal

model. The heat transfer coefficient  $h_{cj}$  is then given by

$$h_{cj} = \frac{\text{Nu}_{cj}\lambda_w}{d_h} \quad (16)$$

where  $\text{Nu}_{cj}$  is obtained by linear interpolation between (13) and (15) in the transition region  $2300 < \text{Re}_w < 4000$ .

Models for the heat transfer through the air gap (ag) between the rotor and the stator are reviewed in [25]. Typically, the flow in the air gap is characterized by the Taylor number  $\text{Ta}$ . For narrow gaps, i.e., if the difference between the outer radius  $r_o$  and the inner radius  $r_i$  of the gap is small, it can be formulated as

$$\text{Ta}_{ag} = \frac{\omega^2 r_i (r_o - r_i)^3}{\nu_{air}^2}. \quad (17)$$

Here,  $\omega$  is the angular velocity of the rotor, and  $\nu_{air}$  describes the kinematic viscosity of air. In [26], different flow regimes that are characterized by the Taylor number  $\text{Ta}$  are distinguished for the Nusselt number

$$\text{Nu}_{ag}(\text{Ta}_{ag}) = \begin{cases} 2\eta_3, & \text{Ta}_{ag} \leq 1994 \\ a_{ag} \text{Ta}_{ag}^{b_{ag}}, & 1994 < \text{Ta}_{ag} < 1.10^4 \\ 0.409\eta_4 \text{Ta}_{ag}^{0.241}, & \text{Ta}_{ag} \geq 1.10^4 \end{cases} \quad (18)$$

where the choice  $a_{ag} = \frac{\text{Nu}_{ag}(1994) - \text{Nu}_{ag}(10^4)}{1994 + 10^4}$ , and  $b_{ag} = \frac{\ln \text{Nu}_{ag}(1994) - \ln \text{Nu}_{ag}(10^4)}{\ln(1994) - \ln 10^4}$  yields a continuous  $\text{Nu}_{ag}$ . Uncertainties of the heat transfer due to, e.g., slotting are taken into account by the factors  $\eta_3$  and  $\eta_4$ , where  $\eta_3 = \eta_4 = 1$  corresponds to the nominal model. The resulting convection coefficient on the inner surface of the stator (radius  $r_i$ ) and the outer surface (radius  $r_o$ ) of the rotor finally reads as [26]

$$h_{ag} = \frac{\lambda_{air}}{2(r_o - r_i)} \text{Nu}_{ag}. \quad (19)$$

The end windings are cooled by oil sprays. A similar cooling concept was studied in [27], where a model that uses circumferential sections of the end winding accounts for the oil velocity's angular dependence. In [27], the Nusselt number  $\text{Nu}_{ew} = 0.664 \text{Re}_{ew}^{\frac{1}{2}} \text{Pr}_{oil}^{\frac{1}{3}}$  is defined by assuming a laminar flow on the surface of the end winding. The main limitation of this model is that detailed knowledge of the fluid velocity on the end winding is required to calculate the Reynolds number  $\text{Re}_{ew}$ . Since these data are not available in the present application, a slightly simplified approach to identify the unknown parameters in the Nusselt relation is derived in this work. First, the average heat transfer coefficients on the lead end winding  $\bar{h}_{ew,le} = \frac{\lambda_{oil}}{d_{o,ew,le}} \text{Nu}_{ew,le}$  and the opposite lead end winding  $\bar{h}_{ew,ole} = \frac{\lambda_{oil}}{d_{o,ew,ole}} \text{Nu}_{ew,ole}$  are introduced, where the respective outer diameters  $d_{o,ew,le}$  and  $d_{o,ew,ole}$  are used as characteristic lengths. Similar to [27], the Nusselt correlations  $\text{Nu}_{ew,le} = 0.664 \text{Re}_{ew,le}^{\frac{1}{2}} \text{Pr}_{oil}^{\frac{1}{3}}$  and  $\text{Nu}_{ew,ole} = 0.664 \text{Re}_{ew,ole}^{\frac{1}{2}} \text{Pr}_{oil}^{\frac{1}{3}}$  are used, where  $\lambda_{oil}$  and  $\text{Pr}_{oil}$  of the oil are evaluated at the oil's inlet temperature  $\vartheta_{oil}$ . In order to

compute the Reynolds numbers  $\text{Re}_{ew,le} = \frac{\bar{v}_{ew,le}(q_{ew,le})d_{o,ew,le}}{\nu_{oil}}$  and  $\text{Re}_{ew,ole} = \frac{\bar{v}_{ew,ole}(q_{ew,ole})d_{o,ew,ole}}{\nu_{oil}}$ , the average fluid velocities  $\bar{v}_{ew,le}$  and  $\bar{v}_{ew,ole}$  are required, respectively. They are functions of the oil flows  $q_{ew,le}$  and  $q_{ew,ole}$  at the end windings but, as stated before, cannot be accurately modeled. Therefore, this relation between the flow rates and the average fluid velocities are approximated by shape-preserving piecewise cubic polynomial interpolation [28]. Six values of the oil flows linearly spaced between the minimum and maximum values  $\mathbf{q}_{ew,le,bp} = [q_{ew,le,1}, \dots, q_{ew,le,6}]^T$  and  $\mathbf{q}_{ew,ole,bp} = [q_{ew,ole,1}, \dots, q_{ew,ole,6}]^T$  are defined. The corresponding average fluid velocities  $\mathbf{v}_{ew,le,bp} = [\bar{v}_{ew,le,1}, \dots, \bar{v}_{ew,le,6}]^T$  and  $\mathbf{v}_{ew,ole,bp} = [\bar{v}_{ew,ole,1}, \dots, \bar{v}_{ew,ole,6}]^T$  will then be identified from measurements on a test machine in Section IV-B.

The construction of the oil distribution rings entails that the wetting of the end windings with oil is worse on the right and left parts ( $\varphi \in [-45^\circ, 45^\circ] \cup [135^\circ, 225^\circ]$ ) compared with the top and bottom parts of the end winding. In order to approximate this effect, an angular dependence of the heat transfer coefficient on the end windings is defined in the form

$$h_{ew,x}(\varphi, q_{ew,x}) = \begin{cases} (2 - \eta_5) \bar{h}_{ew,x}(q_{ew,x}), & \varphi \in [-45^\circ, 45^\circ] \\ & \cup [135^\circ, 225^\circ] \\ \eta_5 \bar{h}_{ew,x}(q_{ew,x}), & \text{otherwise} \end{cases} \quad (20)$$

for the end windings ( $x \in le, ole$ ). The parameter  $\eta_5$  is used to calibrate this model, where  $\eta_5 \in [0, 2]$  ensures that the heat transfer coefficient stays positive on all surfaces. Values  $\eta_5 > 1$  lead to a higher heat transfer coefficient on the top and bottom than the right and left. By identifying this parameter from measurements, the hotspot on the end windings can be captured rather accurately.

The rotor is actively cooled by pumping oil axially through the hollow shaft. In [29], the convective heat transfer coefficient of a similar setup is studied. It is shown that for nonstandstill operation, the heat transfer coefficient is mainly affected by the rotational speed and is almost independent of the flow rate of the oil. The relation  $\text{Nu}_{rs} = c_1 (\text{Re}_{rs} \text{Pr}_{oil})^{c_2}$  with the radial Reynolds number  $\text{Re}_{rs} = \frac{\omega d_{1,rs}^2}{2\nu_{oil}}$ , the Prandtl number  $\text{Pr}_{oil}$ , constants  $c_1 = 3.811 \cdot 10^{-3}$  and  $c_2 = 0.641$ , and the inner diameter of the rotor shaft  $d_{1,rs}$  is proposed in [29]. Based on this model, the heat transfer coefficient  $h_{rs}$  on the inner radial surface of the shaft is defined as

$$h_{rs} = \eta_6 \frac{\lambda_{oil}}{d_{1,rs}} c_1 (\text{Re}_{rs} \text{Pr}_{oil})^{c_2} \quad (21)$$

where the factor  $\eta_6$  is again identified from measurements in Section IV-B. In the present motor design, the oil volume flow is supplied by a fixed displacement pump that is coupled with the rotor (i.e., at a standstill, the flow rate is zero). Thus, this model will also give meaningful results for the standstill, where the heat transfer to the oil can be neglected without losing accuracy. Convection from the rotor shaft to the enclosed

air is neglected here due to the small axial cross sections and the air's low thermal conductivity compared with the oil.

### E. POWER LOSSES

The conversion between electrical power and mechanical power generates heat in the machine, involving copper losses  $P_{Cu}$ , iron core losses  $P_{core}$ , permanent magnet losses  $P_{pm}$ , and mechanical losses  $P_{mech}$ . As copper and core losses dominate [30], mechanical losses are neglected ( $P_{mech} \approx 0$ ).

The total dc power losses for the three phases in the winding are given by

$$P_{Cu,dc}(\bar{\vartheta}_{Cu}) = 3i^2 R_{s,ref} (1 + \alpha_{Cu} (\bar{\vartheta}_{Cu} - \vartheta_{ref})) \quad (22)$$

where  $i = \frac{1}{\sqrt{2}} \sqrt{i_d^2 + i_q^2}$  is the fundamental wave rms current, with the measured currents  $i_d$  and  $i_q$  transformed to the rotor fixed dq-frame using the amplitude-invariant Park transform. The stator resistance  $R_{s,ref}$  at the reference temperature  $\vartheta_{ref}$  is identified from measurements at a standstill. Here,  $\alpha_{Cu}$  is the temperature coefficient of electrical resistivity of the winding. The dc losses (22) are distributed between active winding  $P_{dc,aw}(\bar{\vartheta}_{aw})$  and losses  $P_{ew,le,dc}(\bar{\vartheta}_{ew,le})$  and  $P_{ew,ole,dc}(\bar{\vartheta}_{ew,ole})$  in both end windings, determined by their respective copper masses and average temperatures  $\bar{\vartheta}_{aw}$ ,  $\bar{\vartheta}_{ew,le}$ , and  $\bar{\vartheta}_{ew,ole}$ , respectively. Due to strong magnetic fields in the stator slots [30], the resistance  $R_s$  and, therefore, the losses increase with the electrical frequency  $f_{el} = pn$  of the magnetic field (number of pole-pairs  $p$ , rotational speed of the rotor  $n = \frac{\omega}{2\pi}$ ). Analogously to [30], the model

$$P_{aw}(\bar{\vartheta}_{aw}) = P_{aw,dc}(\bar{\vartheta}_{aw}) \left( 1 + \frac{k_{ac}(f_{el})}{(1 + \alpha_{Cu}(\bar{\vartheta}_{aw} - \vartheta_{ref}))^\beta} \right) \quad (23)$$

is used for the copper losses in the active winding. The function  $k_{ac}(f_{el})$  and the exponent  $\beta$  are identified from finite element analysis to model the skin and proximity effect. Given the weaker magnetic field in the end windings compared with the active winding [31], the factor  $k_{ac}$  is generally much smaller, leading to its omission for the end windings (i.e.,  $P_{ew,le} = P_{ew,le,dc}$  and  $P_{ew,ole} = P_{ew,ole,dc}$ ).

Core losses  $P_{core}$  in the stator and rotor laminations are computed using a Jordan loss model [32]

$$P_{core} = k_{hyst} B^2(i_d, i_q, \bar{\vartheta}_{pm}) f_{el} + k_{eddy} B^2(i_d, i_q, \bar{\vartheta}_{pm}) f_{el}^2 \quad (24)$$

This model uses the empirical factors  $k_{hyst}$  and  $k_{eddy}$  for hysteresis and eddy currents, respectively, along with the local flux density magnitudes  $B(i_d, i_q, \bar{\vartheta}_{pm})$  from FEA results. To facilitate real-time computation,  $k_{hyst} B^2(i_d, i_q, \bar{\vartheta}_{pm})$  and  $k_{eddy} B^2(i_d, i_q, \bar{\vartheta}_{pm})$  are precomputed and spatially lumped, allowing for efficient interpolation to evaluate the lumped losses as defined in (24). Eddy currents due to harmonics in the field are the main source of the losses  $P_{pm}$  in the magnets. These are also obtained from FEA, where the effects of time harmonics in the current are accounted for by empirical factors depending on the operating point.

Local values  $g_i$  of heat generated by losses per unit volume are needed in (2). A uniform loss distribution within the active

winding (aw), end windings (ew, le, ew, and ole), stator teeth (st), stator yoke (sy), rotor lamination stack (r), and permanent magnet (pm), as defined in Section II-C is assumed. For all regions  $r \in \mathcal{R} = \{aw, ew, le, ew, ole, st, sy, r, pm\}$ , the local rate

$$g_i = \frac{P_r(\bar{\vartheta}_r)}{\sum_{j \in \chi_r} V_j} \quad (25)$$

for volume  $i$  is obtained by dividing the total power dissipated in the region that volume  $i$  belongs to  $P_r(\bar{\vartheta}_r)$  by the overall volume of the region  $\sum_{j \in \chi_r} V_j$ . In this context,  $\chi_r$  defines the set of all volume indices associated with region  $r$ . The dissipated power  $P_r$  is calculated by evaluating the lumped loss models (22)–(24) and is in general temperature dependent.

### F. STATE-SPACE FORMULATION

For a compact notation, the overall model is written in matrix notation. The state vector  $\mathbf{x} = [\vartheta_1, \dots, \vartheta_N]^T$  is introduced, which contains the temperatures of the individual finite volumes. The sum of the heat flows  $\sum_j Q_{ij}$  in (2), defined by (3) and (5), also needs to be represented as a vector  $\mathbf{Q}^T = [\sum_j Q_{1j}, \dots, \sum_j Q_{Nj}]$ . For this task, the input vector

$$\mathbf{u}_1^T = [q_w \quad \vartheta_w \quad \mathbf{q}_{oil}^T \quad \vartheta_{oil} \quad n] \quad (26)$$

with  $\mathbf{q}_{oil}^T = [q_{ew,le}, q_{ew,ole}]^T$  is defined. The derivations in the previous sections showed that the heat transfer coefficient  $h_{jk}$  [and thus the thermal conductances (5)] to the water  $\mathbf{G}_w$  (16), to the oil  $\mathbf{G}_{oil}$  (20), and across the airgap  $\mathbf{G}_{ag}$  (19) depend on  $\mathbf{u}_1$ . They are summarized in the vector

$$\mathbf{G}(\mathbf{u}_1) = [\mathbf{G}_w^T(q_w, \vartheta_w) \quad \mathbf{G}_{oil}^T(\mathbf{q}_{oil}, \vartheta_{oil}) \quad \mathbf{G}_{ag}^T(n)]^T \quad (27)$$

of length  $N_G$ , which allows  $\mathbf{Q}$  to be written in the form

$$\mathbf{Q} = \mathbf{A}\mathbf{x} + \sum_{m=1}^{N_G} \mathbf{G}_m(\mathbf{u}_1) \mathbf{N}_m \mathbf{x} + \mathbf{B}_q \mathbf{q}(\mathbf{u}_1) \quad (28)$$

with

$$\mathbf{q}(\mathbf{u}_1) = \begin{bmatrix} \mathbf{G}_w(q_w, \vartheta_w) \vartheta_w \\ \mathbf{G}_{oil}(\mathbf{q}_{oil}, \vartheta_{oil}) \vartheta_{oil} \end{bmatrix} \quad (29)$$

and constant matrices  $\mathbf{A}$ ,  $\mathbf{N}_m$ ,  $m = 1, \dots, N_G$ , and  $\mathbf{B}_q$ . The rates at which heat is generated per volume defined in (25) are summarized in the vector

$$\mathbf{g}^T(\mathbf{u}_2, \vartheta_{avg}) = [g_{aw}(\bar{\vartheta}_{aw}), \dots, g_{pm}(\bar{\vartheta}_{pm})] \quad (30)$$

which depends on the inputs

$$\mathbf{u}_2^T = [i_d \quad i_q \quad n]. \quad (31)$$

The average temperatures  $\vartheta_{avg}$  for a region  $r$  are given by

$$\bar{\vartheta}_r = \frac{\sum_{j \in \chi_r} \vartheta_j V_j}{\sum_{j \in \chi_r} V_j} \quad (32)$$

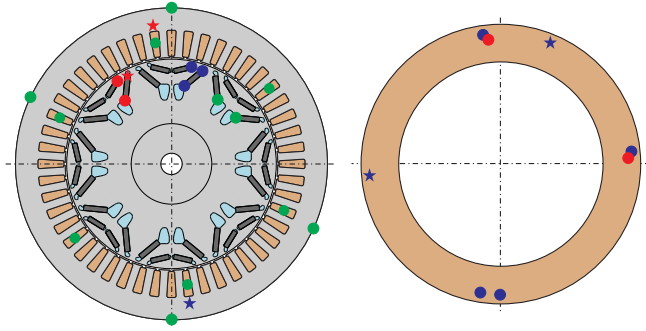


**FIGURE 4.** Temperature sensor locations in the machine: Dot-shaped sensors are for model calibration, while star-shaped ones are for validation only. Colors represent axial positions: blue markers indicate sensors on the lead end side, green markers in the center, and red markers on the opposite side of the lead end.

and the vector of average temperatures can be written as

$$\bar{\vartheta}_{\text{avg}} = \left[ \bar{\vartheta}_{\text{aw}}, \dots, \bar{\vartheta}_{\text{pm}} \right]^T = \mathbf{C}_{\text{avg}} \mathbf{x}. \quad (33)$$

The terms  $g_i V_i$  in (2) can then be written as  $\mathbf{B}_g \mathbf{g}(\mathbf{u}_2, \mathbf{C}_{\text{avg}} \mathbf{x})$ .

With these definitions, the model defined by (2) is written in the form

$$\mathbf{M} \dot{\mathbf{x}} = \mathbf{A} \mathbf{x} + \sum_{m=1}^{N_G} G_m(\mathbf{u}_1) \mathbf{N}_m \mathbf{x} + \mathbf{B} \begin{bmatrix} \mathbf{q}(\mathbf{u}_1) \\ \mathbf{g}(\mathbf{u}_2, \mathbf{C}_{\text{avg}} \mathbf{x}) \end{bmatrix} \quad (34)$$

with  $\mathbf{B} = [\mathbf{B}_q \quad \mathbf{B}_g]$ . The entries on the diagonal of the positive definite mass matrix  $\mathbf{M}$  are given by  $C_i$  from (2). As the differential equation (34) is stiff, it is discretized in time using the implicit trapezoidal method with a sampling time  $T_s = 0.5$  s. This results in the implicit system of equations

$$\mathbf{0} = \mathbf{F}(\mathbf{x}_{k+1}, \mathbf{x}_k, \mathbf{u}_{1,k+1}, \mathbf{u}_{2,k+1}, \mathbf{u}_{1,k}, \mathbf{u}_{2,k}). \quad (35)$$

Here, the subscript  $k$  denotes the corresponding quantity evaluated at the time  $kT_s$ , i.e.,  $\mathbf{x}_k = \mathbf{x}(kT_s)$ .

### G. MODEL OUTPUTS

Every local or averaged temperature at certain locations can be calculated as a linear combination of the states  $\mathbf{x}$ . For model calibration and validation, the temperatures measured by the temperature sensors are of particular interest. The considered machine is instrumented with numerous K-type thermocouples not present in a production sample to allow for detailed model validation.

Six sensors are placed in the stator slots to measure the active winding temperature, see Fig. 4. Another six sensors are mounted in the stator yoke, where four are positioned closer to the cooling jacket, and two of them (star-shaped symbols in Fig. 4) closer to the winding. The end windings are instrumented with six sensors that are distributed around the circumference on the lead end and two sensors on the opposite lead end. The permanent magnet temperatures are measured with temperature sensors in the pockets. All sensors except the star-shaped ones in Fig. 4 are used for the calibration in

Section IV-B. These sensors are later used for the validation of the calibrated model. The temperatures utilized for the model calibration and validation are represented as

$$\mathbf{y}_{\text{sens}} = \mathbf{C}_{\text{sens}} \mathbf{x}. \quad (36)$$

The temperatures utilized only for model validation are calculated as

$$\mathbf{y}_{\text{val}} = \mathbf{C}_{\text{val}} \mathbf{x}. \quad (37)$$

Finally, for the model calibration and the discussion of the results in Section IV-C, the averaged temperatures of the sensors of a component (e.g., the active winding) are relevant. They are calculated as

$$\bar{\mathbf{y}}_{\text{sens}} = \bar{\mathbf{C}}_{\text{sens}} \mathbf{x} \quad (38)$$

where averaging of the values obtained by each sensor within a certain component is used. For example,  $\bar{\vartheta}_{\text{aw,sens}}$  is obtained by averaging all elements in  $\vartheta_{\text{aw,sens}}$ .

### III. MODEL-ORDER REDUCTION

For the discretization visualized in Fig. 3 in Section II-B, the resulting FOM (34) has  $N = 11931$  states. Due to its high memory requirements and computational complexity, the model (34) is unsuitable for real-time implementation on the target platform. Thus, model-order reduction is applied to the model (34). This reduction aims to decrease both memory requirements and computational complexity substantially. At the same time, the model-order reduction is designed to retain the physical interpretation of the thermal conductances while maintaining the input–output characteristics of the model as well as possible. To do so, the expression  $\mathbf{g}(\mathbf{u}_2, \vartheta_{\text{avg}})$  [cf., (23) and (24)] in (34) is linearized with respect to  $\mathbf{x}$  at  $\mathbf{x}_1$ . Here,  $\mathbf{x}_1$  is selected to represent a temperature within the operational range of the machine, specifically a uniform temperature distribution at 80 °C. This yields a model that is bilinear in the inputs  $\mathbf{G}(\mathbf{u}_1)$  and  $\frac{\partial}{\partial \mathbf{x}} \mathbf{g}(\mathbf{u}_2, \mathbf{C}_{\text{avg}} \mathbf{x}_1)$ . The resulting model is evaluated at  $L$  specific sampling points of  $\mathbf{u}_1$ , yielding an affine model. The choice of sampling points aims to minimize the approximation error caused by model-order reduction at these points, while also achieving good agreement between the sampling points. The order of this model is reduced with an iterative rational Krylov algorithm [33] that uses projection matrices  $\mathbf{V}_l$  and  $\mathbf{W}_l$ ,  $l = 1, \dots, L$ . The matrices for different sampling points  $1, \dots, L$  are concatenated to global basis matrices  $[\mathbf{V}_1, \dots, \mathbf{V}_L]$  and  $[\mathbf{W}_1, \dots, \mathbf{W}_L]$ , see [34]. Finally, a singular value decomposition is applied, and columns corresponding to small singular values are removed, yielding the  $N \times N_r$  matrices  $\mathbf{V}$  and  $\mathbf{W}$ . The ROM

$$\mathbf{M}_r \dot{\mathbf{x}}_r = \mathbf{A}_r \mathbf{x}_r + \sum_{m=1}^{N_G} G_m(\mathbf{u}_1) \mathbf{N}_{r,m} \mathbf{x}_r + \mathbf{B}_r \begin{bmatrix} \mathbf{q}(\mathbf{u}_1) \\ \mathbf{g}(\mathbf{u}_2, \mathbf{C}_{r,\text{avg}} \mathbf{x}_r) \end{bmatrix} \quad (39)$$

follows by multiplying (34) from the left-hand side with  $\mathbf{W}^T$  and setting  $\mathbf{x} \approx \mathbf{V} \mathbf{x}_r$ . The thermal conductances  $G_m(\mathbf{u}_1)$  as well as the inputs  $\mathbf{q}(\mathbf{u}_1)$  and  $\mathbf{g}(\mathbf{u}_2, \mathbf{C}_{r,\text{avg}} \mathbf{x}_r)$  are preserved during this step and retain their physical interpretation. This



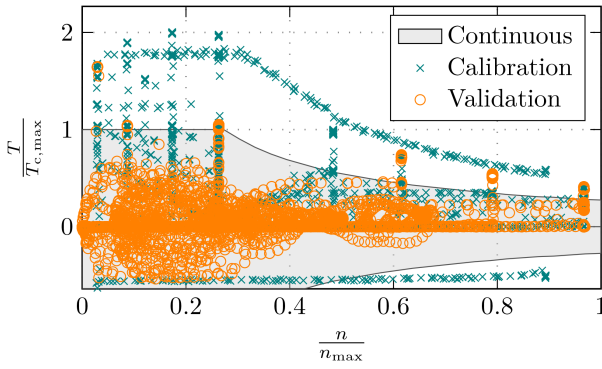


**FIGURE 5.** Considered operating points during model calibration and validation.

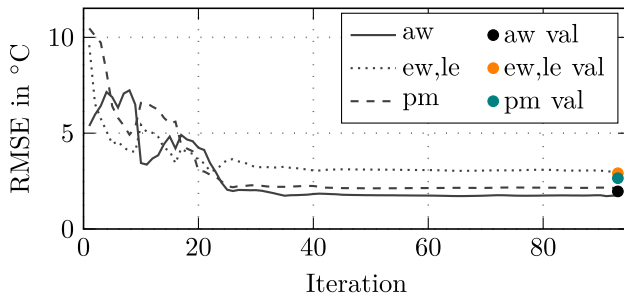


**FIGURE 6.** RMSE evaluated based on the calibration data during model calibration. The dots indicate the performance of the calibrated model evaluated based on the validation data.

allows to systematically consider varying thermal conductances at the boundaries, e.g., due to the variations of the flow rates of the coolant in the ROM. The parameters  $\eta_1, \dots, \eta_6$ ,  $\mathbf{v}_{ew,le,bp}$ , and  $\mathbf{v}_{ew,ole,bp}$  are preserved, allowing model calibration based on these (uncertain) parameters in the ROM.<sup>1</sup> All matrices in the model (39) can be computed offline once the basis matrices  $\mathbf{V}$  and  $\mathbf{W}$  are known, allowing efficient model evaluation. The temperatures at the sensor positions and the average temperatures needed for (30) are obtained from (36) and (33) as  $\mathbf{C}_{sens,r}\mathbf{x}_r = \mathbf{C}_{sens}\mathbf{V}\mathbf{x}_r$  and  $\mathbf{C}_{avg,r}\mathbf{x}_r = \mathbf{C}_{avg}\mathbf{V}\mathbf{x}_r$ , respectively. Compared with the FOM, the number of states can be significantly reduced ( $N_r = 10 \ll N = 11\,931$ ).

#### IV. EXPERIMENTAL RESULTS

In this section, measurement results are compared with simulation results of the FOM and the ROM.

##### A. EXPERIMENTAL SETUP AND METHODOLOGY

In total, 78 experiments for 57 h including both continuous and peak loads are available. Fig. 5 shows the operating range covered by the measurements and data allocation for calibration and validation. Here, torque and speed are normalized to the maximum speed,  $n_{max}$ , and the maximum

continuous torque,  $T_{c,max}$ . These measurements correspond to operating scenarios that test whether the machine fulfills the performance requirements. During the experiments, the water flow rates  $q_w$  and the fluid temperatures are also varied. The operating points correspond to tests with constant speed and torque, followed by cool down periods (see Fig. 9), resulting in overlapping points in Fig. 5, and representative drive cycles (such as in Fig. 12). Fig. 5 shows that validation data also cover peak performance data not within the envelope of continuous power operating points and that the validation data extend to areas where calibration data are absent.

The data gathered in these experiments are divided into two sets, with approximately 45 h allocated for calibration (see Section IV-B) and 12 h for validation.

##### B. MODEL CALIBRATION

As mentioned in Sections II-C and II-D, not all material parameters and boundary conditions can be accurately obtained by the available geometry and material parameters of the PMSM. The 22 uncertain parameters

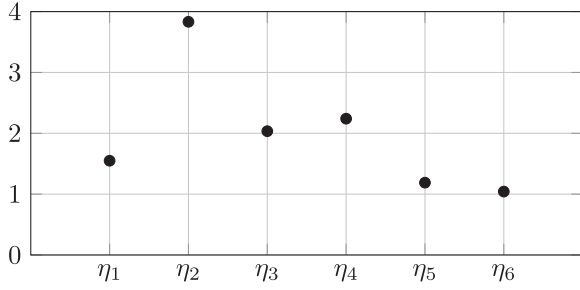
$$\mathbf{p} = [\lambda_{aw,pl} \quad \lambda_{ew,ax} \quad \lambda_{ew,rad} \quad \lambda_{ew,az} \quad \eta_1 \quad \dots \quad \eta_6 \quad \mathbf{v}_{ew,le,bp}^T \quad \mathbf{v}_{ew,ole,bp}^T]^T. \quad (40)$$

defined in Section II-C, (16), (18), (20), and (21) are identified from the calibration data. The calibration experiments  $j = 1, \dots, M$  with the corresponding measured inputs  $\mathbf{u}_{1,k}^j$  and  $\mathbf{u}_{2,k}^j$  according to (26), (31), and the measured temperatures  $\mathbf{y}_{sens,k}^{m,j}$  of the instrumented machine in Section II-G are recorded for  $k = 0, \dots, L_j$ . For the calibration, the error  $\mathbf{e}_k^j = \mathbf{y}_{sens,k}^{m,j} - \mathbf{y}_{sens,k}^j$  between the measured and the simulated temperatures of the FOM  $\mathbf{y}_{sens,k}^j = \mathbf{C}_{sens}\mathbf{x}_k^j$  is defined, with the state  $\mathbf{x}_k^j$  predicted by the FOM at time  $kT_s$ . Due to the potential nonideal contact of a temperature sensor and component, it is useful to also define the error of the average measured component temperature as  $\bar{\mathbf{e}}_k^j = \bar{\mathbf{y}}_{sens,k}^{m,j} - \bar{\mathbf{y}}_{sens,k}^j$ . For the identification of  $\mathbf{p}$ , the optimization problem

$$\begin{aligned} \min_{\mathbf{p}} \quad & \sum_{j=1}^M \sum_{k=1}^{L_j} \left( \|\bar{\mathbf{e}}_k^j\|_{\bar{\mathbf{W}}}^2 + \gamma \|\mathbf{e}_k^j\|_{\mathbf{W}}^2 \right) dt. \\ \text{s.t.} \quad & (35), \mathbf{x}_0 = \mathbf{x}_0^j, \mathbf{u}_{1,k} = \mathbf{u}_{1,k}^j, \mathbf{u}_{2,k} = \mathbf{u}_{2,k}^j \\ & j = 1, \dots, M \\ & \underline{\mathbf{p}} \leq \mathbf{p} \leq \bar{\mathbf{p}} \end{aligned} \quad (41)$$

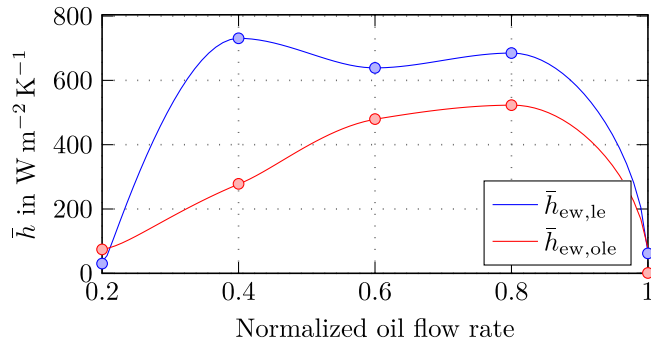
is formulated. In the cost function, the square of the errors  $\bar{\mathbf{e}}_k^j$  and  $\mathbf{e}_k^j$  are weighted with  $\bar{\mathbf{W}}$ ,  $\mathbf{W}$ , and  $\gamma$ , respectively. In order to ensure a low error, especially for the permanent magnet, the active winding, and the end winding, the weights  $\bar{\mathbf{W}}$  and  $\mathbf{W}$  are chosen as diagonal matrices with higher weights (factors 2 and 1) for the permanent magnets and the winding compared with the remaining sensors (factor 0.5). The weighting between the average component and the individual sensor

<sup>1</sup>In order to also preserve, e.g., the thermal conductivities as parameters in the ROM, e.g., a linearization of  $\mathbf{A}$ ,  $\mathbf{N}_m$ , and  $\mathbf{B}$  in (34) with respect to those quantities is required.


**FIGURE 7.** Values of normalized identified parameters.

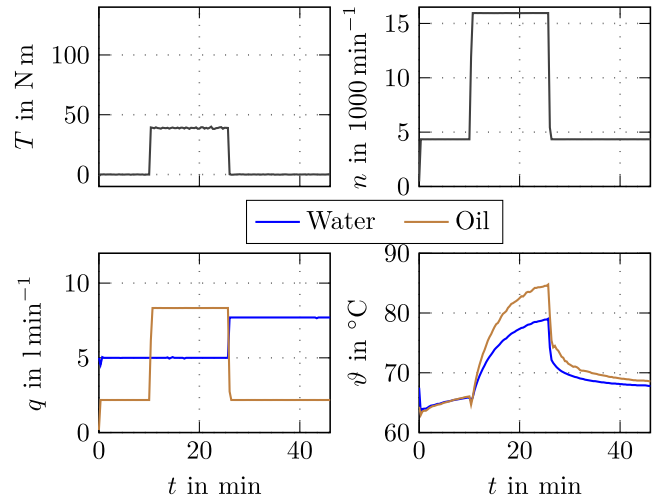
**TABLE 2.** Identified Thermal Conductivities

	Unit	Initial	Identified
$\lambda_{aw,pl}$	$\text{W m}^{-1} \text{K}^{-1}$	0.85	2.1
$\lambda_{ew,ax}$	$\text{W m}^{-1} \text{K}^{-1}$	0.53	1.6
$\lambda_{ew,rad}$	$\text{W m}^{-1} \text{K}^{-1}$	0.53	12.9
$\lambda_{ew,az}$	$\text{W m}^{-1} \text{K}^{-1}$	169	0.83

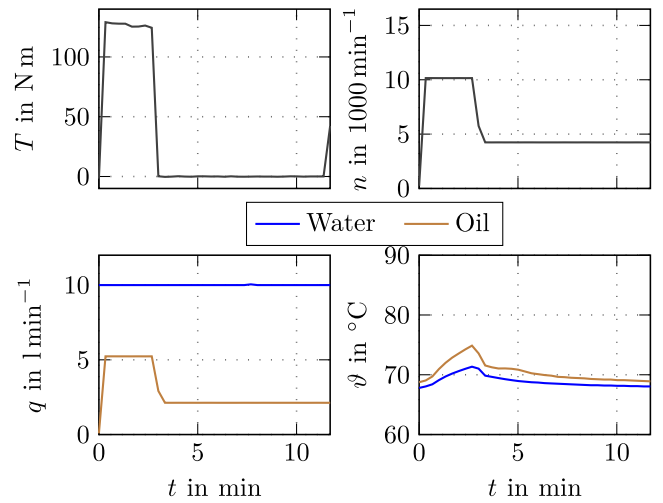

**FIGURE 8.** Identified heat transfer coefficients for the end windings.

temperatures can be adjusted by  $\gamma$ . The initial state  $\mathbf{x}_0^j$  is approximated by assigning the temperature of the closest sensor within the respective material to each volume. The bounds  $\underline{\mathbf{p}} \leq \mathbf{p} \leq \overline{\mathbf{p}}$  ensure that parameters, such as thermal conductivities and heat transfer coefficients, are kept within reasonable limits. The discretized model (35) is used to solve the optimization problem (41). All parameters are scaled with their nominal value such that the cost is approximately equally sensitive to changes in any parameter. The optimization problem (41) is solved using the interior point method. The gradient of the cost in (41) with respect to  $\mathbf{p}$  is computed using the adjoint equation approach [35].

The root-mean-squared errors (RMSEs) of the average temperatures of the active winding (aw), the lead end winding (ew,le), and permanent magnets (pm) evaluated based on the calibration data during model calibration are depicted in Fig. 6. The initial uncalibrated model exhibits RMSEs of approximately 5.4 °C, 9.6 °C, and 10.5 °C for the active winding, the end winding, and the permanent magnets, respectively. After approximately 90 iterations the optimizer finds an optimum. The dots in Fig. 6 indicate the performance of the



(a)



(b)

**FIGURE 9.** Input signals for two exemplary experiments. (a) Experiment 1. (b) Experiment 2.

calibrated model evaluated based on the validation data, showing similar RMSEs as evaluated based on the calibration data. To prevent only a local optimum from being found, the optimization is started from multiple starting points. Although, it always resulted in the same optimal parameter set. A detailed discussion of optimal parameter values is provided in the subsequent paragraph. The obtained optimal values are within physically meaningful ranges, which confirms the quality of the obtained optimum.

The normalized parameters  $\eta_1, \dots, \eta_6$  were all initialized to one. Their identified values are shown in Fig. 7. While  $\eta_5$  and  $\eta_6$  are close to their nominal value, higher deviations are obtained for the other parameters. This can be attributed to the fact that  $\eta_1$  and  $\eta_2$  are related to the heat transfer to the cooling jacket, and  $\eta_3$  and  $\eta_4$  are used within the model of the heat transfer over the air gap. These motor parts are challenging to model, e.g., due to deviations in the friction factor (13), the

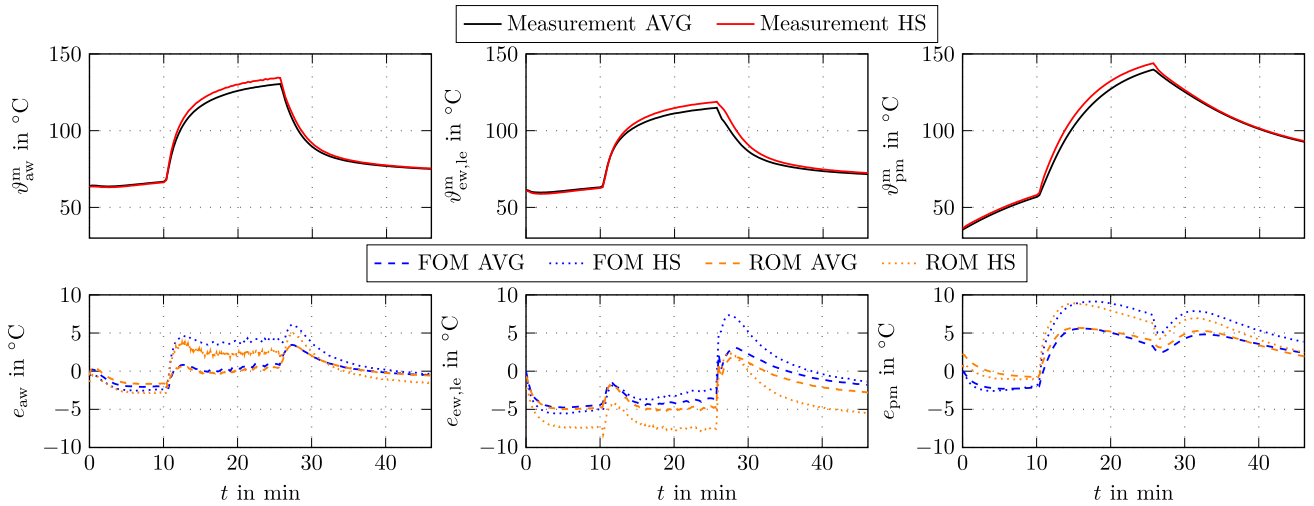


FIGURE 10. Experiment 1 defined in Fig. 9(a): Comparison of the errors in the average and the hotspot temperature of the FOM and the ROM.

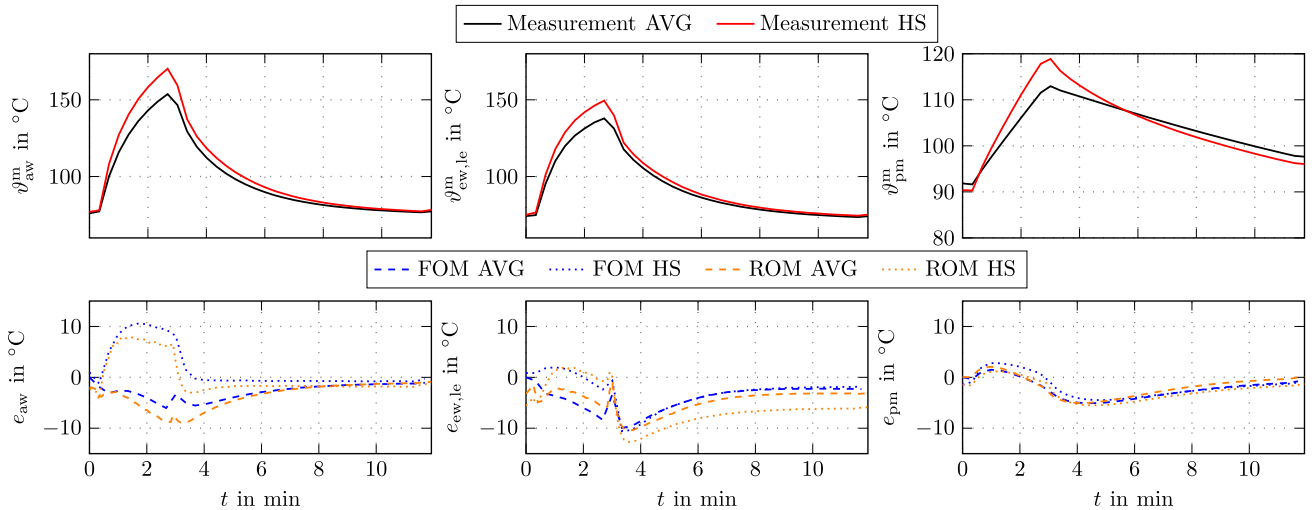
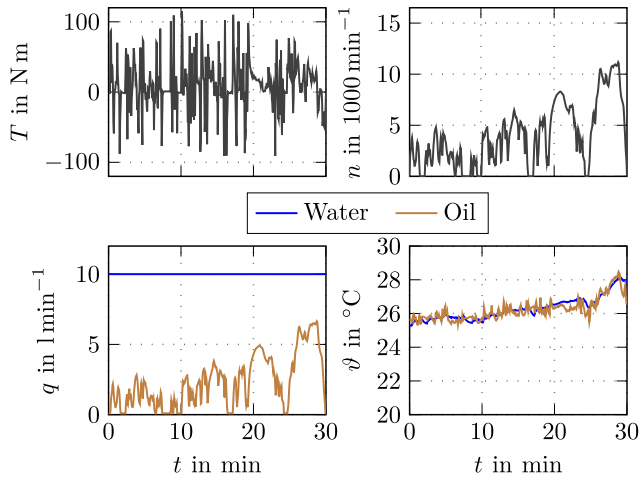


FIGURE 11. Experiment 2 defined in Fig. 9(b): Comparison of the errors in the average and the hotspot temperature of the FOM and the ROM.

contact conductance between the stator lamination stack and the cooling jacket  $h_{c,ls,cj}$ , and the flow behavior within the air gap.

The identified thermal conductivities are compared with their initial values in Table 2. The identified in-plane thermal conductivity in the active winding is approximately 2.5 times the estimated value by the model (10). A deviation in that size was expected due to uncertainties resulting, e.g., from the conductor placement and the impregnation quality, see Section II-C. The thermal conductivities of the end winding show significant deviations from the initial model assumption as outlined in Section II-C. Although the wires are mainly oriented in the azimuthal direction, the conductivity  $\lambda_{ew,az}$  is comparatively low. The reason might be that the end windings are made of individual wire bundles insulated against

each other via resin and insulation material, therefore reducing the effective thermal conductivity. For the heat transfer coefficients of the end windings, the optimization was initialized with a linear relationship between the average velocities and the flow rates  $\mathbf{v}_{ew,le,bp} = \frac{1}{A_{c,le}} \mathbf{q}_{ew,le,bp}$  and  $\mathbf{v}_{ew,ole,bp} = \frac{1}{A_{c,ole}} \mathbf{q}_{ew,ole,bp}$ . Here,  $A_{c,le}$  and  $A_{c,ole}$  denote constant initial estimates for the film thickness of the oil on the two end windings. The identified average heat transfer coefficients  $\bar{h}_{ew,le}(q_{ew,le})$  and  $\bar{h}_{ew,ole}(q_{ew,ole})$  on both end windings are shown in Fig. 8 as functions of the normalized oil flow rate. For the end winding on the lead end side is generally higher than for the opposite side. This can be attributed to a higher oil flow at the lead end due to its higher volume, including the leads. Both heat transfer coefficients show a decrease above 0.8. This unexpected behavior could result from increased



**FIGURE 12.** Excitation signals for a driving cycle.

oil splashing away from the end winding, reducing the heat transfer coefficient. Another explanation is an unmodeled oil distribution effect that effectively decreases the oil flow to the end windings even though the total oil flow increases.

In total, the required computation time for the optimization is approximately 264 h, utilizing eight cores on a machine with Intel Xeon Gold 5154 processor at 3.0 GHz in MATLAB/Simulink 2021b. The computations for the model calibration can be carried out offline and are, therefore, less critical in terms of computational demand. The performance of this calibrated model is discussed in detail in the following Section IV-C.

### C. VALIDATION AND COMPARISON

The identified parameters are used for all following simulations. After the calibration according to Section IV-B, the model-order reduction is performed. A single sampling point  $\mathbf{u}_1$  at nominal operating conditions of the cooling systems and intermediate speed ( $q_W = 10 \text{ min}^{-1}$ ,  $\vartheta_W = \vartheta_{oil} = 65^\circ\text{C}$ ,  $q_{ew,le} = 0.5\max(q_{ew,le})$ ,  $q_{ew,ole} = 0.5\max(q_{ew,ole})$ , and  $n = 8000 \text{ min}^{-1}$ ) is used to construct the global basis for the projection matrices. Accurate results between the FOM and ROM across all operational regions can be achieved with the single sampling point at the center of the operational range. The ROM with  $N_r = 10$  states is discretized in time using an explicit Euler scheme with a sampling time of 500 ms. The implicit trapezoidal rule with a sampling time of 500 ms is used for the FOM.

The inputs  $\mathbf{u}_1$  (26) and the torque  $T$  for two exemplary experiments of the validation data are shown in Fig. 9. The currents needed for the input (31) are selected according to a maximum torque per ampere map for the given torque and speed. The oil flow is the sum of the oil flows to the end windings, the rotor shaft, and a gear box. Both experiments contain a phase where the motor is loaded with torque once at a continuous power, as shown in Fig. 9(a), and once at a peak power operating point, as shown in Fig. 9(b). The fluid temperatures  $\vartheta_w$  and  $\vartheta_{oil}$  start at approximately  $65^\circ\text{C}$  and

increase when the load is applied. The fluid flow rate  $q_w$  is varied during the continuous power operating point, as shown in Fig. 9(a).

This section evaluates the average (AVG) and hotspot (HS) temperatures to assess the model's accuracy. The hotspot temperature of a specific component (e.g., the active winding) is defined as the measured temperature  $\vartheta_{aw,sens,k}^m$  of the sensor  $k$ , where the highest temperature of the component occurs during the cycle, i.e.,  $k = \text{argmax}_k \vartheta_{aw,sens,k}^m$ .

In Figs. 10 and 11, the measured temperatures of the active winding (aw), the end winding lead end (ew,le), and the permanent magnet (pm) are shown for the two experiments of Fig. 9. These temperatures are of specific interest since excessive temperatures can yield insulation failures of the winding and demagnetization of the permanent magnets. Therefore, they need to be accurately predicted by the thermal model. The errors  $e$  in the average and hotspot between measurement and simulation are depicted for the FOM and the ROM. For the experiment in Fig. 11, there is a significant difference between the average and hotspot temperature for the winding and the magnets, which can be attributed to the high power. For the experiment in Fig. 11, the difference is smaller due to the lower power and higher oil flow rate. The error in the average temperatures computed by the FOM and ROM is less than  $10.5^\circ\text{C}$  for the active winding and the end winding for the continuous and peak power operating point. Moreover, the errors in the hotspot temperature are kept below  $13^\circ\text{C}$  for both experiments. For the permanent magnet, the error of the average and hotspot temperatures are below 6 and  $9.5^\circ\text{C}$ , respectively. Comparing the FOM and the ROM reveals similar errors, with a maximum deviation between the models of  $\approx 4^\circ\text{C}$  even at peak power operation. Thus, it can be concluded that the model-order reduction effectively maintains the high model accuracy of the FOM for both stationary and dynamic operations across various operating conditions.

The experiments depicted so far cover cases with very high load changes. These test cases are particularly suitable for analyzing the machine's behavior under maximum load conditions. However, these cases rarely occur in real operations. Thus, the thermal behavior of the machine is analyzed for a driving cycle similar to a worldwide harmonised light-duty vehicles test procedure (WLTP) test cycle.

The corresponding input signals are shown in Fig. 12, and the measurements as well as the results of the models are given in Fig. 13. Due to the lower initial temperature and overall lower powers, the measured temperatures in Fig. 13 are significantly lower than in the high load scenarios. The accuracy of both models for this driving cycle is quite good, keeping the model error below  $5^\circ\text{C}$  for the whole time. Moreover, the ROM has almost the same accuracy as the FOM. This shows that the proposed ROM gives accurate results in real-world dynamic cycles.

As discussed in Section I, low-order LPTN models are the state-of-the-art solution for real-time thermal modeling of automotive electric drive systems. Thus, the proposed models are compared with a low-order LPTN with seven nodes (see, e.g., [36]), see Fig. 14. The seven nodes correspond

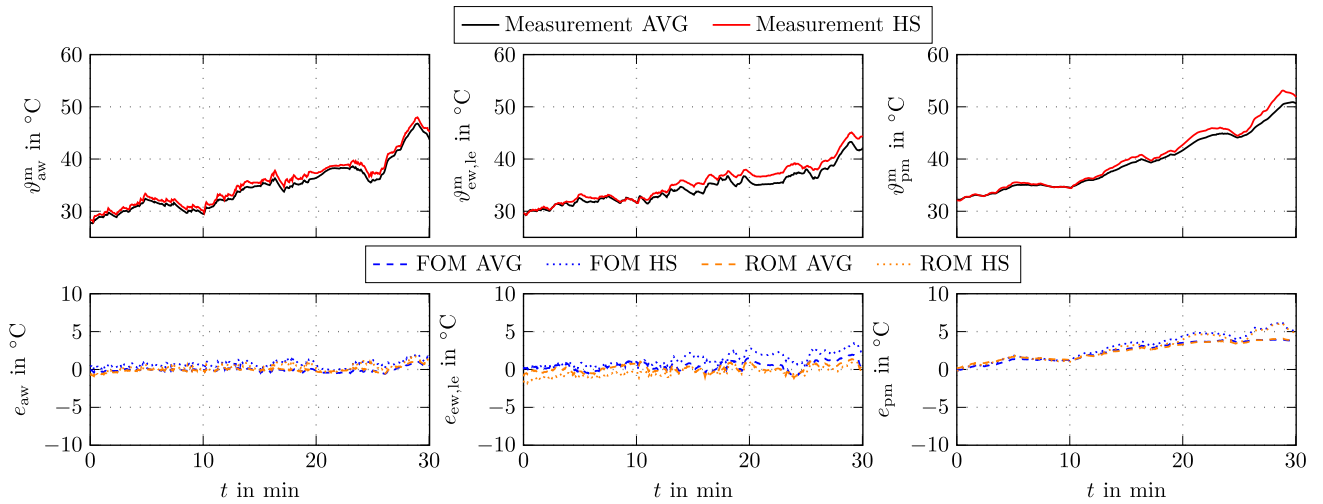


FIGURE 13. Experiment defined in Fig. 12: Comparison of the errors in the average and the hotspot temperature of the FOM and the ROM.

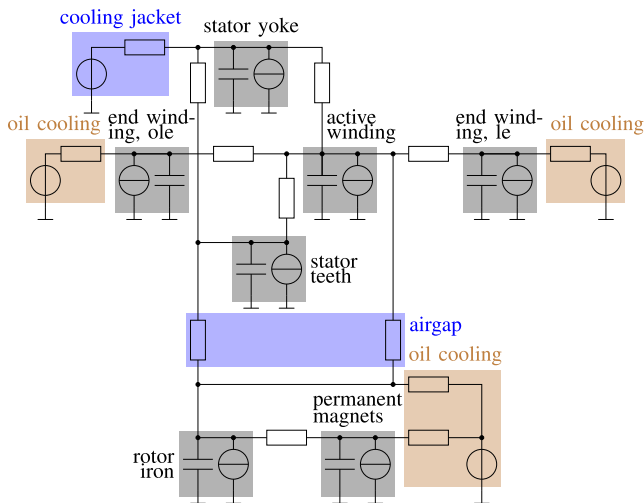


FIGURE 14. Schematic of the LPTN.

to the average temperatures of the stator yoke, stator teeth, active winding, permanent magnet, rotor iron, and end windings (lead end and opposite lead end) and are highlighted with a gray background in Fig. 14. Varying resistances corresponding to convective heat transfer have a blue or brown background, whereas constant resistances are shown without a background color. As proposed in [10], the thermal resistances corresponding to convective heat transfer depending on the speed or the flow rates (see Section II-D), are modeled in the form  $R_{ij} \exp(-\frac{q}{q_{\max}} \frac{1}{b_{ij}}) + a_{ij}$  and  $R_{ij} \exp(-\frac{n}{n_{\max}} \frac{1}{b_{ij}}) + a_{ij}$ , with the flow rate  $q$ , the speed  $n$ , and the corresponding maximum values  $q_{\max}$  and  $n_{\max}$ . The parameters  $R_{ij}$ ,  $a_{ij}$ , and  $b_{ij}$  as well as constant thermal resistances and the thermal capacities are identified from measurements using the same cost function as in Section IV-B. This results in an overall number of 34 parameters of the LPTN. The same loss model as in Section II-E is used for the LPTN. Like the ROM, the

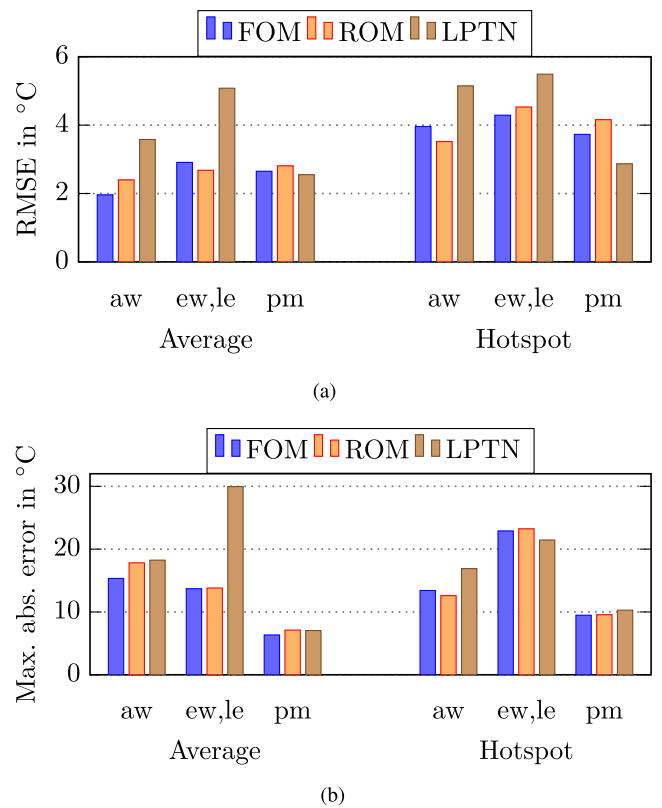
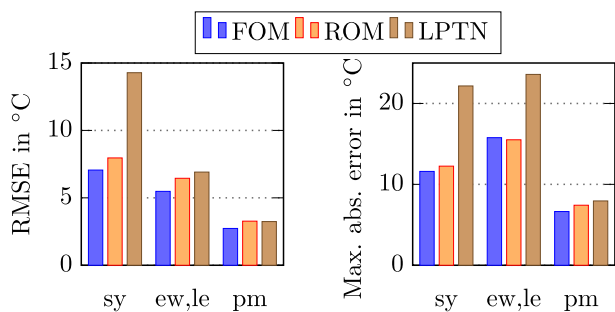


FIGURE 15. (a) RMSEs and (b) maximum absolute errors computed with the validation data for the active winding (aw), the end winding at the lead end (ew,le), and the permanent magnets (pm).

resulting calibrated LPTN model is discretized in time with an explicit Euler method using a sampling time of 500 ms.

Fig. 15(a) shows the RMSEs of the validation data for the different models for average and hotspot temperature at the active winding, the end winding, and the permanent magnet. As expected, the FOM and ROM show a similar performance, with only minor differences. The LPTN gives



**FIGURE 16.** RMSEs of the temperatures at the locations of the validation sensors on the stator yoke (sy), the end winding (ew,le), and the permanent magnets (pm).

larger errors, particularly for the end windings, where the average maximum absolute error reaches 30 °C. The accuracy for the permanent magnet temperature is of similar quality for all considered models. These results confirm that 1) the ROM is suitable to reach an almost identical accuracy as the FOM, and 2) the proposed model gives good results for all critical components of the motor, whereas the LPTN shows less accurate results for the end windings.

An important advantage of the proposed model compared with LPTNs is that it is possible to predict the temperature field of the whole machine. Thus, if temperatures other than those at the sensor positions are of interest, they can be easily added as outputs of the model as shown in Section II-G, without increasing the number of states. To prove that the proposed FOM and ROM yield high accuracy for positions where no sensor was utilized for the model calibration, the temperatures of the validation sensors depicted as stars in Fig. 4 are analyzed [model outputs (37)]. The measured temperatures corresponding to the model outputs (37) were not used in the model calibration of Section IV-B. In order to show that the models can predict the temperature even though no calibration was performed, the RMSE and the maximum absolute error of the average measured temperatures for the validation sensors  $\bar{y}_{val}^m$  on the stator yoke (sy), the end winding (ew), and the permanent magnets (pm) evaluated based on the validation data are shown in Fig. 16. There, the FOM and the ROM utilize temperatures from the specific sensor positions, whereas the LPTN relies on the temperature of the corresponding node representing that region. For the FOM and the ROM, the RMSE and the maximum absolute error are below 8 and 14 °C, respectively. For the LPTN, the errors are significantly higher, especially for the stator yoke and the end winding at the lead end side. This indicates that the assumption of homogeneous temperature is invalid for these regions. For the permanent magnets, the three methods perform similar, which may root in the rather homogeneous temperature of this part of the motor. This result also shows that LPTNs that fit to measurement data can only accurately predict the temperature of those nodes where the model is calibrated. If the temperature at another position must be predicted, the

model has to be extended by an additional node and recalibrated.

Section I already described that the model's real-time capability on automotive real-time hardware is one essential requirement of the thermal model. To evaluate the computing time of the FOM, the ROM, and the LPTN, a cycle of 1 h duration is analyzed. All simulations are performed on a desktop computer with an AMD Ryzen 7 5800X processor at 3.8 GHz in MATLAB/Simulink 2021b.<sup>2</sup> The FOM requires 486 s, the ROM 13.3 s, and the LPTN 5.4 s. As expected, the FOM has the highest and the LPTN the lowest computing time, whereas the ROM is only approximately 2.5 times slower than the LPTN. Since it is known that the LPTN is real-time capable on automotive hardware, the ROM is also well suited for real-time temperature prediction. For performance assessment, the ROM is implemented on a dSpace MicroLabBox prototyping system, with NXP QorIQ P5020 processor @2 GHz resulting in a computing time of approximately 0.1 ms per timestep. This corresponds to 0.02% of the sampling time of 0.5 s allocated to the ROM and suggests real-time capability of the implementation, leaving sufficient computational resources for other tasks.

The advantages of the ROM compared with the LPTN thus make the ROM a promising alternative to classical LPTNs.

## V. CONCLUSION

A thermal model of a PMSM was developed based on the geometry, the material parameters, and empirical correlations for the boundary conditions. The finite-volume method was applied for spatial discretization, and measurements calibrated the resulting model. The formulation of the model in a bilinear structure was exploited to obtain an efficient model-order reduction scheme, which is required to ensure the real-time capability of the model. This specific formulation further preserves the physical interpretation of the inputs and certain parameters, allowing the ROM to cover changing cooling conditions. The experimental validation of the method for a machine using water and oil cooling showed that a ROM with ten states yields highly accurate results for real-time temperature prediction. Compared with a state-of-the-art LPTN, lower errors emerge especially for the active and end winding. Moreover, it is demonstrated that the proposed model enables accurate temperature prediction at locations where no sensor was positioned during model calibration. Future work is directed toward using the model in designing a nonlinear observer that combines, e.g., the measurements of (a low number of) temperature sensors with temperature estimates resulting from the measurements in the electric system (e.g., the back-electromotive force). With this, the overall prediction accuracy is expected to be further improved.

<sup>2</sup>Although this configuration does not provide a good value for the implementation on an automotive real-time hardware, it allows us to compare the different modeling approaches.

## ACKNOWLEDGMENT

The authors would like to thank Magna Powertrain GmbH & Co KG for supporting the research work. The authors acknowledge TU Wien Bibliothek for financial support through its Open Access Funding Programme.

## REFERENCES

- [1] P.-O. Gronwald and T. A. Kern, "Traction motor cooling systems: A literature review and comparative study," *IEEE Trans. Transport. Electrification*, vol. 7, no. 4, pp. 2892–2913, Dec. 2021.
- [2] E. Brancato, "Estimation of lifetime expectancies of motors," *IEEE Elect. Insul. Mag.*, vol. 8, no. 3, pp. 5–13, May/June 1992.
- [3] T. Sebastian, "Temperature effects on torque production and efficiency of PM motors using NdFeB magnets," *IEEE Trans. Ind. Appl.*, vol. 31, no. 2, pp. 353–357, Mar./Apr. 1995.
- [4] P. H. Mellor and D. R. Turner, "Real time prediction of temperatures in an induction motor using a microprocessor," *Electric Machines Power Syst.*, vol. 15, no. 4/5, pp. 333–352, 1988.
- [5] B. Bilgin et al., "Modeling and analysis of electric motors: State-of-the-art review," *IEEE Trans. Transport. Electrification*, vol. 5, no. 3, pp. 602–617, Sep. 2019.
- [6] C. Jungreuthmayer et al., "A detailed heat and fluid flow analysis of an internal permanent magnet synchronous machine by means of computational fluid dynamics," *IEEE Trans. Ind. Electron.*, vol. 59, no. 12, pp. 4568–4578, Dec. 2012.
- [7] O. Wallscheid, "Thermal monitoring of electric motors: State-of-the-art review and future challenges," *IEEE Open J. Ind. Appl.*, vol. 2, pp. 204–223, 2021.
- [8] T. Meng and P. Zhang, "A review of thermal monitoring techniques for radial permanent magnet machines," *Machines*, vol. 10, no. 1, 2021, Art. no. 18.
- [9] R. Wrobel and P. H. Mellor, "A general cuboidal element for three-dimensional thermal modelling," *IEEE Trans. Magn.*, vol. 46, no. 8, pp. 3197–3200, Aug. 2010.
- [10] O. Wallscheid and J. Bocker, "Global identification of a low-order lumped-parameter thermal network for permanent magnet synchronous motors," *IEEE Trans. Energy Convers.*, vol. 31, no. 1, pp. 354–365, Mar. 2016.
- [11] D. Liang et al., "A hybrid lumped-parameter and two-dimensional analytical thermal model for electrical machines," *IEEE Trans. Ind. Appl.*, vol. 57, no. 1, pp. 246–258, Jan./Feb. 2021.
- [12] W. Kirchgassner, O. Wallscheid, and J. Bocker, "Data-driven permanent magnet temperature estimation in synchronous motors with supervised machine learning: A benchmark," *IEEE Trans. Energy Convers.*, vol. 36, no. 3, pp. 2059–2067, Sep. 2021.
- [13] A. Bruns and P. Benner, "Parametric model order reduction of thermal models using the bilinear interpolatory rational Krylov algorithm," *Math. Comput. Modelling Dynamical Syst.*, vol. 21, no. 2, pp. 103–129, 2014.
- [14] K. Zhou, J. Pries, and H. Hofmann, "Computationally-efficient 3 D finite-element-based dynamic thermal models of electric machines," in *Proc. Int. Electric Machines Drives Conf.*, 2013, pp. 839–846.
- [15] F. Qi, D. A. Ly, C. van der Broeck, D. Yan, and R. W. D. Doncker, "Model order reduction suitable for online linear parameter-varying thermal models of electric motors," in *Proc. Annu. Southern Power Electron. Conf.*, 2016, pp. 1–6.
- [16] A. Miyamoto, H. Sauerland, H. Xu, and R. W. De Doncker, "Automatic model order reduction technique for real-time temperature monitoring of oil-cooled electric machines," *IEEE Trans. Ind. Appl.*, vol. 60, no. 1, pp. 477–485, Jan./Feb. 2023.
- [17] T. L. Bergman, A. S. Lavine, F. P. Incropera, and D. P. DeWitt, *Fundamentals of Heat and Mass Transfer*, 8th ed. Hoboken, NJ, USA: Wiley, 2017.
- [18] S. Patankar, *Numerical Heat Transfer and Fluid Flow*, 1st ed. Boca Raton, FL, USA: CRC Press, 2018.
- [19] A. J. Grobler, S. R. Holm, and G. van Schoor, "Empirical parameter identification for a hybrid thermal model of a high-speed permanent magnet synchronous machine," *IEEE Trans. Ind. Electron.*, vol. 65, no. 2, pp. 1616–1625, Feb. 2018.
- [20] D. Staton, A. Boglietti, and A. Cavagnino, "Solving the more difficult aspects of electric motor thermal analysis in small and medium size industrial induction motors," *IEEE Trans. Energy Convers.*, vol. 20, no. 3, pp. 620–628, Sep. 2005.
- [21] J. E. Cousineau, K. Bennion, D. DeVoto, and S. Narumanchi, "Experimental characterization and modeling of thermal resistance of electric machine lamination stacks," *Int. J. Heat Mass Transfer*, vol. 129, pp. 152–159, 2019.
- [22] N. Simpson, R. Wrobel, and P. H. Mellor, "Estimation of equivalent thermal parameters of impregnated electrical windings," *IEEE Trans. Ind. Appl.*, vol. 49, no. 6, pp. 2505–2515, Nov./Dec. 2013.
- [23] B. Groschup, M. Nell, F. Pauli, and K. Hameyer, "Characteristic thermal parameters in electric motors: Comparison between induction- and permanent magnet excited machine," *IEEE Trans. Energy Convers.*, vol. 36, no. 3, pp. 2239–2248, 2021.
- [24] *VDI Heat Atlas*, 2nd ed. Berlin, Germany: Springer, 2010.
- [25] D. A. Howey, P. R. N. Childs, and A. S. Holmes, "Air-gap convection in rotating electrical machines," *IEEE Trans. Ind. Electron.*, vol. 59, no. 3, pp. 1367–1375, Mar. 2012.
- [26] K. M. Becker and J. Kaye, "Measurements of diabatic flow in an annulus with an inner rotating cylinder," *J. Heat Transfer*, vol. 84, no. 2, pp. 97–104, 1962.
- [27] S. Nategh, Z. Huang, A. Krings, O. Wallmark, and M. Leksell, "Thermal modeling of directly cooled electric machines using lumped parameter and limited CFD analysis," *IEEE Trans. Energy Convers.*, vol. 28, no. 4, pp. 979–990, Dec. 2013.
- [28] C. B. Moler, *Numer. Comput. with MATLAB*. Philadelphia, PA, USA: SIAM, 2004.
- [29] Y. Gai et al., "Numerical and experimental calculation of CHTC in an oil-based shaft cooling system for a high-speed high-power PMSM," *IEEE Trans. Ind. Electron.*, vol. 67, no. 6, pp. 4371–4380, Jun. 2020.
- [30] R. Wrobel, P. H. Mellor, M. Popescu, and D. A. Staton, "Power loss analysis in thermal design of electrical machines," in *Proc. Workshop Elect. Machines Des. Control Diagnosis*, 2015, pp. 118–126.
- [31] R. Wrobel, A. Mlot, and P. H. Mellor, "Contribution of end-winding proximity losses to temperature variation in electromagnetic devices," *IEEE Trans. Ind. Electron.*, vol. 59, no. 2, pp. 848–857, Feb. 2012.
- [32] S. Xue et al., "Iron loss model for electrical machine fed by low switching frequency inverter," *IEEE Trans. Magn.*, vol. 53, no. 11, pp. 1–4, Nov. 2017.
- [33] S. Gugercin, A. C. Antoulas, and C. Beattie, " $\mathcal{H}_2$  model reduction for large-scale linear dynamical systems," *SIAM J. Matrix Anal. Appl.*, vol. 30, no. 2, pp. 609–638, 2008.
- [34] P. Benner, S. Gugercin, and K. Willcox, "A survey of projection-based model reduction methods for parametric dynamical systems," *SIAM Rev.*, vol. 57, no. 4, pp. 483–531, 2015.
- [35] M. Gerdts, *Optimal Control of ODEs and DAEs*. Berlin, Germany: De Gruyter, 2012.
- [36] J. Feng, D. Liang, Z. Q. Zhu, S. Guo, Y. Li, and A. Zhao, "Improved low-order thermal model for critical temperature estimation of PMSM," *IEEE Trans. Energy Convers.*, vol. 37, no. 1, pp. 413–423, Mar. 2022.



**MARTIN STEFAN BAUMANN** received the Dipl.-Ing. degree in electrical engineering from TU Wien, Wien, Austria, in 2021.

He is currently a Research Assistant with the Automation and Control Institute, TU Wien. His research interests include modeling, identification, and observer design for temperature prediction in electric machines.



**ANDREAS STEINBOECK** received the M.Sc. degree in mechatronics from Loughborough University, Loughborough, U.K., in 2005, the Dipl.-Ing. degree in mechatronics from Johannes Kepler University, Linz, Austria, in 2007, and the Ph.D. degree in electrical engineering and the habilitation degree in systems theory and control from TU Wien, Vienna, Austria, in 2011 and 2020, respectively.

He is an Associate Professor for advanced control of industrial production processes with TU Wien. His current research interests include mathematical modeling, identification, optimization, control of nonlinear dynamical systems, model predictive control, and advanced process control with applications in production processes, and mechatronic systems.



**WOLFGANG KEMMETMÜLLER** (Member, IEEE) received the Dipl.-Ing. degree in mechatronics from Johannes Kepler University, Linz, Austria, in 2002, the Ph.D. (Dr. Ing.) degree in control engineering from Saarland University, Saarbrücken, Germany, in 2007, and the habilitation degree in system theory and automatic control from TU Wien, Vienna, Austria, in 2017.

He is currently an Associate Professor with the Automation and Control Institute, TU Wien.

His research interests include physics-based modeling and nonlinear control of mechatronic systems with a special focus on power electronics, electrohydraulic, and electromechanical systems.



**ANDREAS KUGI** (Senior Member, IEEE) received the Dipl.-Ing. degree in electrical engineering from TU Graz, Graz, Austria, in 1992, and the Ph.D. degree in control engineering and the habilitation degree in automatic control and control theory from Johannes Kepler University (JKU), Linz, Austria, in 1995 and 2000, respectively.

He was an Associate Professor with JKU from 2000 to 2002 and a Full Professor with Saarland University, Saarbrücken, Germany, from 2002 to 2007. Since 2007, he has been a Full Professor

of complex dynamical systems with Automation and Control Institute, TU Wien, Vienna, Austria. From 2017 to 2023, he was the Head of the Center for Vision, Automation, and Control, AIT Austrian Institute of Technology GmbH, Vienna, where since July 2023, he has been the Scientific Director. His main research interests include modeling, control, and optimization of complex dynamical systems, mechatronic system design, and robotics and process automation.

Dr. Kugi is a Full Member of the Austrian Academy of Sciences and a Member of the German National Academy of Science and Engineering (acatech).